GDCh Research Articles Angewandte Chemie International Edition www.angewandte.org

Advanced Oxidation Processes

How to cite:
International Edition: doi.org/10.1002/anie.202202338
German Edition: doi.org/10.1002/ange.202202338

Cobalt Single Atoms Anchored on Oxygen-Doped Tubular Carbon Nitride for Efficient Peroxymonosulfate Activation: Simultaneous Coordination Structure and Morphology Modulation

Ziwei Wang, Eydhah Almatrafi, Han Wang, Hong Qin, Wenjun Wang, Li Du, Sha Chen, Guangming Zeng, and Piao Xu**

Abstract: Simultaneous regulation of the coordination environment of single-atom catalysts (SACs) and engineering architectures with efficient exposed active sites are efficient strategies for boosting peroxymonosulfate (PMS) activation. We isolated cobalt atoms with dual nitrogen and oxygen coordination ($Co–N_3O_1$) on oxygen-doped tubular carbon nitride (TCN) by pyrolyzing a hydrogen-bonded cyanuric acid melamine–cobalt acetate precursor. The theoretically constructed $Co–N_3O_1$ moiety on TCN exhibited an impressive mass activity of 7.61×10^5 $min^{-1} mol^{-1}$ with high $^1O_2$ selectivity. Theoretical calculations revealed that the cobalt single atoms occupied a dual nitrogen and oxygen coordination environment, and that PMS adsorption was promoted and energy barriers reduced for the key *O intermediate that produced $^1O_2$. The catalysts were attached to a widely used poly(vinylidene fluoride) microfiltration membrane to deliver an antibiotic wastewater treatment system with 97.5 % ciprofloxacin rejection over 10 hours, thereby revealing the suitability of the membrane for industrial applications.

Introduction

Advanced oxidation processes (AOPs), especially for the peroxymonosulfate (PMS) activation, are state-of-the-art wastewater treatment technologies for water decontamination.[1] Its removal of recalcitrant organic contaminants relies on the highly reactive radicals ($^{\bullet}OH$ and $SO_4^{\bullet-}$) or alternative nonradical pathways.[2] Among the alternative nonradical pathways, singlet oxygenation has received tremendous attention as its intrinsic advantages of long life, wide pH tolerance, strong electrophilicity and selectivity.[3] As a result, singlet oxygenation in PMS-AOPs displays high selectivity toward electron-rich organic substances or bacteria and maintains excellent efficiency in complicated environmental interference.[4] In general, the singlet oxygen ($^1O_2$) forms via self-decay, nucleophilic addition, and catalytic activation of peroxy acids like PMS.[5] Many carbonaceous materials such as carbon nanotubes[6] and biochar[7] as well as transition metal-based catalysts[8] are efficient activators for PMS-AOPs towards $^1O_2$ generation, but the process is usually accompanied by the production of free radicals such as $^{\bullet}OH$ and $SO_4^{\bullet-}$. Furthermore, their practical application in environment remediation still suffers from poor stability, low atomic utilization efficiency, and slow activation kinetics.

Co single-atom catalysts (SACs) with atomically dispersed active sites are one of the most promising catalysts for PMS-AOPs due to significantly promoted catalytic properties, well-defined structure and the highest reactivity of Co^{2+}.[9] Firstly, compared to metal nanocrystals or oxides, single atoms possess greater atomic utilization and mass activity toward PMS activation.[8,10] For example, the reaction rate of Co–N–C single atoms on tetrapyridomacrocyclic support for PMS activation is 2 to 4 orders of magnitude higher than that of Co^{2+} and Co_3O_4 catalysts.[11] Secondly, the rational design of SACs can further modulate the reaction pathway towards $^1O_2$ production.[9a] Lately, the transformation of $Co–N_4–C$ structure to $Co–N_{2+2}–C$ coordination has obtained with more than 98 % $^1O_2$ generation selectivity for PMS activation.[12] Therefore, defining single-atom sites at an atomic level and constructing the macrostructures of the whole catalyst can synergistically enhance PMS-AOPs catalytic efficiency and $^1O_2$ production selectivity. However, the investigation of the structure-property relationships is highly fascinating yet difficult.

In general, the catalytic performance of Co–SACs is simultaneously determined by isolated metal atoms, their local coordination environment and support architectures.[13] The N atoms on the support not only anchor the metal atoms but also modulate the electronic structures of the active centers.[14] Therefore, the replacement of N atoms with other atoms (e.g. O and S) can alter the electronic structure of the active sites, further promoting the turnover

---

[*] Dr. Z. Wang, Dr. H. Wang, Dr. H. Qin, Dr. W. Wang, Dr. L. Du, Dr. S. Chen, Prof. G. Zeng, Prof. P. Xu
College of Environmental Science and Engineering, Hunan University and Key Laboratory of Environmental Biology and Pollution Control (Ministry of Education), Hunan University
Changsha 410082 (P. R. China)
E-mail: zgming@hnu.edu.cn
piaoxu@hnu.edu.cn

Prof. E. Almatrafi, Prof. G. Zeng, Prof. P. Xu
Centre of Research Excellence in Renewable Energy and Power Systems, Center of Excellence in Desalination Technology, Department of Mechanical Engineering, Faculty of Engineering-Rabigh, King Abdulaziz University
Jeddah 21589 (Saudi Arabia)

frequencies and boosting catalytic activity.[15] For instance, June et al.[16] synthesized Co single atoms on N, O doped graphene support and Qiao et al.[17] explored the effects of oxygen-adjacent Co single atoms on the oxygen reduction reaction (ORR). These findings verified the optimized Co–N_4 moiety obtained by incorporating O-adjacent C atom displayed superior ORR activity and high H_2O_2 productivity, originating from the active site shift and modulation. Furthermore, the rationally engineering architectures of support can enhance surface area and porosity, thus enabling the maximum exposure of the active sites.[18] In PMS-AOPs, oxygen-doped carbon nitrogen (CN) and Co–SACs (Co–N_4 moiety) both have been studied as efficient catalysts.[10e,19] However, simultaneously modulating the local coordination environment of Co single atoms and support architectures of CN has few been reported regarding PMS-AOPs, which further leads to a poor understanding of reaction mechanisms, and structure-property relationships.

Herein, we designed a supramolecular precursor to prepare isolated Co atoms with N, O-dual coordination on oxygen-doped tubular CN as an effective activator for PMS-AOPs. The single Co atom dispersion and tubular filling-like porous architecture provided abundant exposed active sites and sufficient interaction with PMS as well as related activation intermediates, resulting in high PMS activation ability and selectivity for $^1O_2$ generation. Theoretical calculation revealed that O-adjacent Co–SACs could indeed alter PMS adsorption configuration and reduce energy barriers of key *O intermediate toward $^1O_2$ production. We further illustrated the immobilization of the catalysts in a poly(vinylidene fluoride) microfiltration membrane to establish a continuous flow system. Intriguingly, this study details the insights into the Co–SACs with molecular-level engineering for efficient and sustainable wastewater remediation.

Results and Discussion

It is established that the adsorption energy (E_{ads}) of PMS and the O–O bond length (l_{O-O}) in the PMS molecular have a direct impact on PMS activation.[4,20] Typically, E_{ads} controls the thermodynamic feasibility of an adsorption process and indicates the interactions between catalysts and PMS, while the l_{O-O} reflects the feasibility of PMS cleavage.[21] Therefore, we conducted periodic DFT calculations to investigate the impact of molecular-level local structures of Co–N_4/CN (Co–N_4) catalysts on PMS activation, including the prevalent Co_3O_4, CN, oxygen-doped CN and various configurations of Co–SACs at the molecular level (modulation of the first coordination sphere, such as B, O, S, P, namely Co–N_3B_1, Co–N_3O_1, Co–N_3S_1, Co–N_3P_1). The E_{ads} and l_{O-O} on different models were shown in Figure 1a, Figure S1 and Table S1. We found that PMS was energetically preferred to be adsorbed by Co–N_3O_1 moiety and Co_3O_4, whereas the former Co–SACs prefer breaking the O–O bond of PMS molecule, which leads to active species formation. Additionally, Figure 1b showed the formation energy of Co–N_4 moiety in a unit of g–C_3N_4 and the formation energy of two possible coordination environment (named Co–N_3O_1 and Co–N_4–O) in a unit of oxygen-doped g–C_3N_4. Compared to the Co–N_4 moiety and Co–N_4–O (oxygen in the second coordination sphere), the formation energy of Co–N_3O_1 reduced from 2.14 eV and −2.03 eV to −2.44 eV respectively, indicating a more feasible coordinated position.

Guided by the analysis from theoretical calculations, the attention of this article focused on Co–SACs on oxygen-doped carbon nitride. It was reported that hydrothermal treatment could simultaneously dope oxygen atoms into CN and regulate the architectures.[22] The preparation process was presented in Figure 1c. The melamine supramolecular precursors were synthesized under hydrothermal conditions, which underwent a self-assembly process into hydrogen bonding cyanuric acid-melamine.[23] Then, the supramolecular precursors were calcinated to generate nanotube structure (TCN, height $\approx 1.18\ \mu m$) during high temperature (AFM, Figure 1d, TEM and SEM, Figure S2a). Meanwhile, the coordinated cobaltous nodes were reduced by the generated abundant reductive atmosphere during calcination. Pre-mediated coordination of cobaltous acetate and supramolecular precursors could change the distance of adjacent Co atoms, thus preventing the aggregation of Co atoms and the construction of Co–Co bonds (TEM Figure 1e, f).[24] No clear change of morphology was found after calcination with addition of cobaltous acetate (Figure S2b–f). Furthermore, isolated single Co atoms (assigned by bright spots) were obviously observed anchoring on the internal architecture (HAADF-STEM, Figure 1g, TEM, Figure S3, S4). The engineering support architecture relies on morphology controls (along with oxygen atoms introduction) and subsequently uncoordinated metal-ligand removal from precursors. The incorporation of oxygen atoms into supramolecular precursors provided abundant surface anchoring sites for metal atoms and efficiently reduced the formation energy for Co–SACs.[25] Furthermore, the associated interactions between the precursors and metal atoms finely controlled the spatial location between adjacent Co atoms, which were further in favor of Co–SACs formation.[26] EDS mapping across a part of nanotube (Figure 1h) suggested the homogeneous distribution of N, C, O, Co over Co–N_3O_1 matrix. As proof of concept, the pyrolysis of the precursors synthesized by ball-milling of melamine, cyanuric acid and cobaltous acetate also had the desired effects (Figure S5).

The crystal structures of CN, Co–N_4, TCN, Co–N_3O_1 were illustrated by XRD (Figure S6a). Two characteristic peaks at 13.4° and 27.6° were ascribed to (110) and (200) facets of origin CN. As can be seen, TCN and Co–N_3O_1 maintained the basic skeleton of carbon nitride, which was also proved in the (FT-IR) spectra (Figure S6b). The absence of characteristic peaks of cobalt species, such as cobalt crystal, cobaltous oxides further agreed with HAADF-STEM results. While for TCN and Co–N_3O_1, the reflection peaks of (200) facets shifted to a higher angle, indicating that the incorporation of O heteroatom atoms might distribute the packing of the singlet layers of CN.[27] The enhanced paramagnetic signal with a g value of 2.003

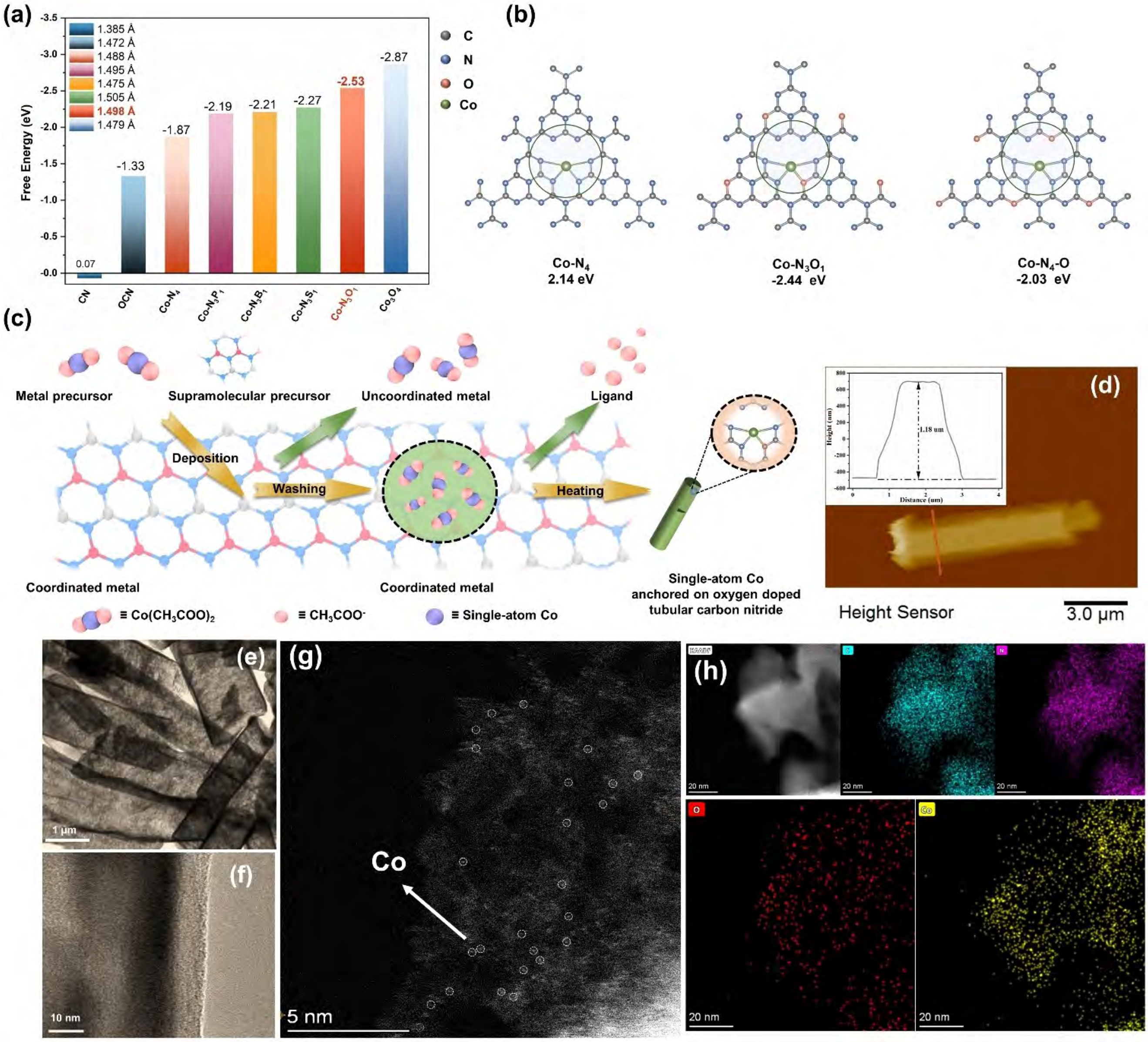

Figure 1. a) The adsorption energy (E_{ads}) of PMS on prevalent Co_3O_4, CN and oxygen-doped CN (OCN) and various configurations at the molecular level of Co–N_4 moiety (in the first coordination sphere, such as B, O, S, P, etc.) and the corresponding O–O bond length (l_{O-O}) in PMS after adsorption (b) Calculated formation energy of Co–N_4 and different O-adjacent Co–SACs (Co–N_3O_1 and Co–N_4–O), c) Process of the formation of Co–N_3O_1, d) AFM of TCN, e), f) TEM images of Co–N_3O_1, g) HAADF-STEM of Co–N_3O_1, h) EDS mapping images of Co–N_3O_1.

further supported that oxygen atoms were introduced into TCN (Figure S7a). The surface area of Co–N_3O_1–3 was 83.11 $m^2 g^{-1}$, which was about 2.08 and 8.33 times than that of TCN and CN (Figure S7b, Table S2). This was because the tubular structure enhanced the accessible surface area and the introduction of Co atoms within the framework generated more porous architecture. According to the ICP-MS measurement, the Co content for Co–N_4, Co–N_3O_1–1, Co–N_3O_1–2 and Co–N_3O_1–3 were 0.99, 0.51, 3.08 and 10.49 wt %, respectively (Table S2).

To investigate the chemical position and electronic structures of CN, TCN Co–N_4 and Co–N_3O_1, XPS spectra was performed. Through the comparison among the high-resolution C 1s, O 1s of CN and TCN, two variations could be observed in this spectrum and were emphasized by differently shaded regions in Figure 2a, b. The peaks at C 1s and O 1s corresponding to C–O groups exhibited a clear increase in the intensity while the C–N=C species existent in TCN was found to be lower than that of CN, confirming that the presence of trace amounts of sp^2-hybridized N atoms substituted by O atoms in the C-containing triazine rings.[28] Several reports have also proved this observation that the doped O atoms are favorable for the substitution of two-coordinated N atoms.[19a] Given the difference in electronegativity between O atoms and N atoms, this change would alter the electronic structure of TCN and further have a

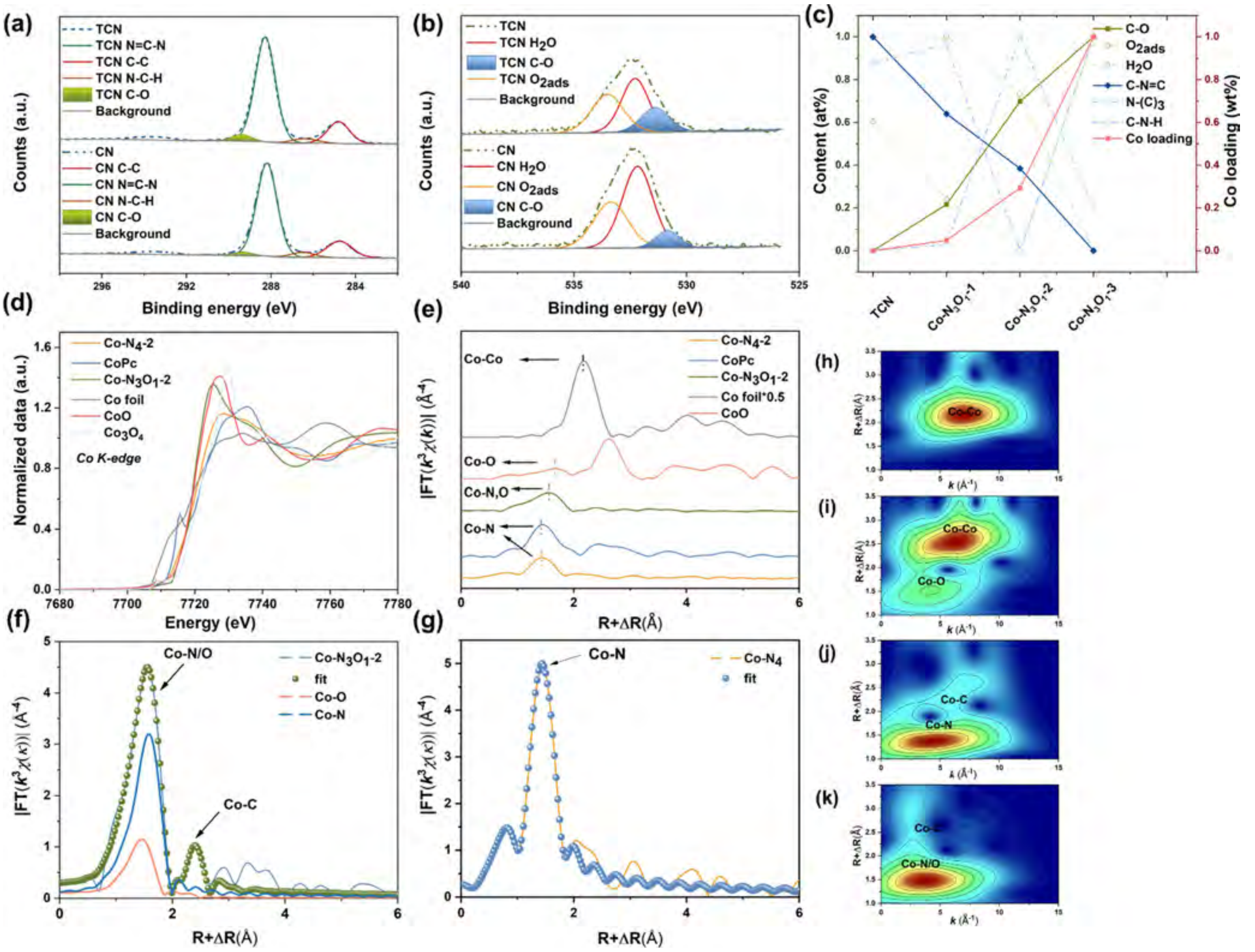

Figure 2. Devolution of a) C 1s, b) O1s XPS spectra of TCN and CN, c) the contents of O and C functions according to XPS and the Co loadings in TCN and Co–N$_3$O$_1$ samples, d) Normalized Co K-edge XANES spectra of Co foil and the Co–based samples e) Co K-edge FT-EXAFS spectra for Co–N$_3$O$_1$, Co–N$_4$ and reference samples. Co K-edge EXAFS fitting analyses for Co–N$_3$O$_1$ (f) and Co–N$_4$ (g) in R space (g), h)–k) Co K-edge WT-EXAFS contour plots for Co–N$_3$O$_1$ and reference samples.

direct impact on the coordination environment of single Co atoms. As shown in Figure S8 and Table S3, correlation of Co loadings with different O and N contents across all TCN matrix-based catalysts revealed that only C–O groups and C–N=C species exhibited a direct trend with Co loadings (the normalization method was adopted), indicating that the nucleation of Co mainly at N, O-dual related sites (Figure 2c). In comparison to Co–N$_3$O$_1$, the Co 2*p* spectrum of Co–N$_4$ displayed a downshift to lower binding energy and the spin-orbit splitting of Co–N$_4$ (15.32 eV) was smaller than that of Co–N$_3$O$_1$–Co (15.81 eV), indicating that Co–N$_3$O$_1$–Co possessed highly oxidized cobalt atom centers with a lower charge density state (Figure S9d).[16]

X-ray absorption fine structure (XAFS) measurements were conducted to identify the possible chemical state and coordination environment of single Co atoms in Co–N$_3$O$_1$ and Co–N$_4$. As shown in Figure 2d, the X-ray absorption near edge structure (XANES) spectra of Co–N$_3$O$_1$, Co–N$_4$ and references compounds indicated that the absorption edge (line position) of single Co atoms was close to that of CoO, suggesting the valence state of Co species in Co–N$_3$O$_1$ r and Co–N$_4$ resemble 2+. The Fourier transform (FT) EXAFS of Co–N$_3$O$_1$, Co–N$_4$ and reference samples revealed that Co species coordinated as isolated single atoms due to the absence of characteristic peaks of Co–Co (at 2.18 Å). Notably, a slight variation in the local coordination structures among samples was observed in FT EXAFS and wavelet transform (WT) analysis (Figure 2h–k) due to the shifts of the major peaks. One major peak (1.56 Å) for Co–N$_3$O$_1$ was located between the backscattering of Co–N (Co–N$_4$, CoPc) and Co–O (CoO), referring to the construction of Co–N, O dual coordination environment. (Figure 2e).[17,19b] Consistent with the FT results, the intensity maximum of Co–N$_3$O$_1$ in WT spectrum displayed a leftward shift, which was possibly assigned to the oxidation of Co atoms. These findings are consistent with proposed structure and a similar coordination configuration reported in 2021.[14a,16,17] To confirm the local coordination configurations in prepared samples, the quantitative least-squares EXAFS curve-fitting analyses were used to reveal the first shell of the Co atom. The detailed fitted parameters and different models were listed in Figure S10, Table S4. As displayed in Figure 2f and 2g, the best fitting results of Co–N_3O_1 showed a four-coordination number and contained Co–N and Co–O backscattering paths, which were different from the coordination environment of Co–N (3.9 ± 0.3) in Co–N_4. The corresponding number for N and O atoms were 3.1 ± 0.5 and 1.0 ± 0.3 at distance of 2.03 and 1.92 Å, suggesting the possible Co–N_3O_1 configuration and further confirming the introduction of O atoms into Co–N_4 moieties.

The catalytic activity of Co–N_3O_1 as PMS-AOPs catalysts was evaluated by the oxidative degradation of CIP as a model reaction. As expected, all Co–N_3O_1 samples exhibited much higher catalytic degradation rate with CIP degradation efficiency up to 100 % within 20 min (Figure 3a). Compared with Co–N_4–1 moiety (with similar Co–Content), the k_{obs} of Co–N_3O_1 increased from 0.0289 min^{-1} to 0.287 min^{-1}. While < 80 % CIP was decomposed when using Co_3O_4 as catalysts and the TCN or pristine PMS displayed negligible catalytic performance. To investigate the catalytic activity based on a quantitative comparison, we normalized the k value based on the mole ratio of metal contents ($k_{per\text{-}site}$), surface area ($k_{surface\ area}$) and used turnover frequency (TOF) to fit CIP degradation process (Table S5).[11] As shown in Figure 3b, the Co–N_3O_1–2 exhibited the highest normalized $k_{per\text{-}site}$ value and TOF efficiency, which was up to 7.61×10^5 $min^{-1} mol^{-1}$ and 0.014 s^{-1}. All the Co–N_3O_1 catalysts possessed a higher normalized $k_{per\text{-}site}$ value and TOF efficiency, indicating that per Co atom in Co–N_3O_1 had a higher reactivity for PMS activation than that of Co–N_4. The significantly enhanced normalized k value and TOF efficiency of Co–N_3O_1 and Co–N_4 structure compared to Co^{2+} and Co_3O_4 could be ascribed to the interaction between oxygen-doped C_3N_4 matrix and single Co active centers.[29] Although the configuration of Co–N_3O_1 presented superior

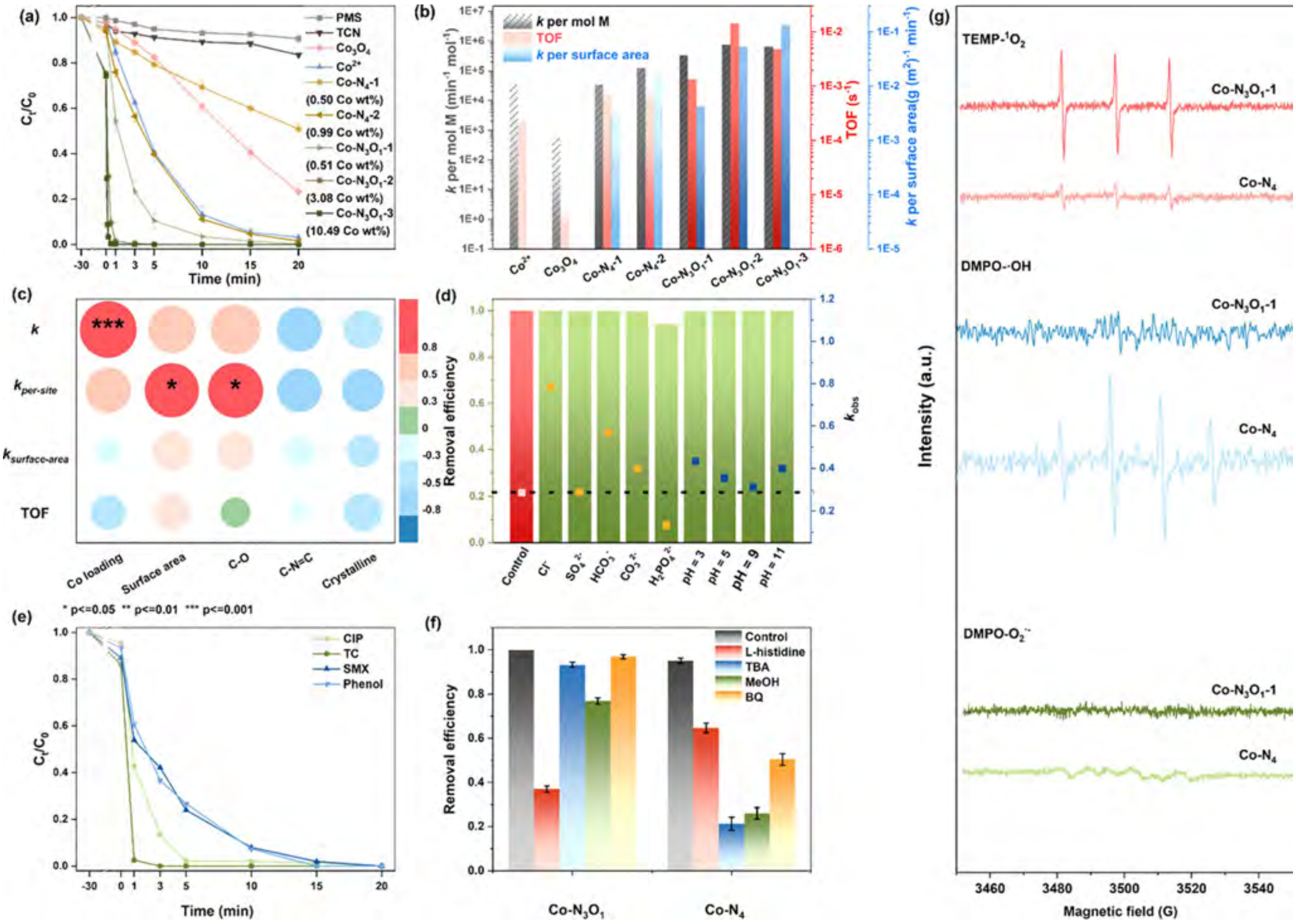

Figure 3. a) Degradation curves of CIP in different catalysts activated PMS systems. [CIP] = 5 mg L^{-1}, [PMS] = 1 mM, catalysts = 0.1 g L^{-1}, T = 298 K, initial solution WpH 6.5. b) Corresponding degradation rate including normalized k value by per mole M atom, per surface area and TOF values. c) Correlation between the effect factors and catalytic performance of catalysts in this PMS-AOPs. d) Removal efficiency and k value in Co–N_3O_1–1 activated PMS system in different pH and the presence of different ions. e) Degradation of various organic contaminants in the Co–N_3O_1–1/PMS system. f) Removal efficiency in the Co–N_3O_1–1/PMS system and Co–N_4/PMS system with different quenchers presented. g) ESR spectra of $^{\bullet}OH$, $SO_4^{\bullet-}$, $O_2^{\bullet-}$, and $^1O_2$. Reaction conditions: [CIP, TC, SMX, Phenol] = 5 mg L^{-1}, [PMS] = 1 mM, catalysts = 0.1 g L^{-1}, Co^{2+} = 5.3 μM, T = 298 K, initial solution pH 6.5, [Cl^-, CO_3^{2-}, HCO_3^-, SO_4^{2-}, $H_2PO_4^-$] = 5 mM, [L-histidine, BQ] = 5 mM, [MeOH, TBA] = 500 mM.

activity towards PMS-AOPs compared to Co–N_4 moieties, some distinct indicators, such as different TOFs among the same configurations and the higher $k_{\text{surface area}}$ value of Co–N_4–2 than that of Co–N_3O_1–1, suggested that other factors may all cause the activity difference.[30]

To further investigate the origins of the catalyst's activity, the potential correlations between the effect factors and catalytic performance of catalysts in these PMS-AOPs were established (Figure 3c).[31] The magnitude and degree of the correlation were represented by the shade of color and the size of circle, respectively. Furthermore, the number of asterisk referred to a significant level. Obviously, the index of Co loading displayed strong positive relevance with k value ($0.8 < R^2 = 0.99 < 1$, $p < = 0.001$). The effects of surface area and C–O species also presented positive correlations with $k_{\text{per-site}}$ ($0.8 < R^2 = 0.90 < 1$, $0.8 < R^2 = 0.93 < 1$, $p < = 0.05$). Therefore, it was reasonable to speculate that Co loading, surface area and C–O species all play critical roles in the improvement of catalytic performance, in which Co atoms were the dominant factor. It should be noted that the preparation of Co–N_3O_1 could modulate the coordination environment and regulate support architecture, thus simultaneously incorporating oxygen atoms into the first shell of Co SACs and enhancing Co loading as well as surface area. As a result, the degradation efficiency of Co–N_3O_1 was higher than most of SACs-based, carbon-derived and g-C_3N_4-based catalysts reported previously (Table S6).

Liquid chromatography–mass spectrometry (LC-MS) was performed to identify the degradation intermediates.[31] As displayed in Figure S11, the chromatograms of a 5 mg L^{-1} CIP solution at different reaction times were presented. The labeled peaks are corresponding to CIP with $m/z = 332$ at retention time 10.7 min and major degradation intermediates with $m/z = 348$ at retention time 4.5 min. The peaks of CIP decayed rapidly with the reaction time finally disappeared after 20 min. The results were consistent with the degradation experiment (Figure 3a). Subsequently, the notable peaks of intermediates enhanced firstly and then decayed along with the increasing reaction time (Figure S12), indicating that the intermediates were broken down into some small molecules and further oxidized into CO_2 and H_2O.[32] Based on the above analysis, a possible degradation pathway was illustrated in Figure S13.

To identify the exceptional stability of Co–N_3O_1, the CIP degradation experiments were repeated five times (Figure S14). All Co–N_3O_1 samples showed excellent cycle stability and Co–N_3O_1–1 still maintained its crystal structure, morphology and isolated Co atoms (Figure S15). Moreover, the residual Co element in Co–N_3O_1–1 after five cycles was 0.41 wt %, which was 80.4 % of that in the origin catalysts (Table S2). Besides, the catalytic activity of Co–N_3O_1–1 was applicable to a wide pH range of 3–11 and various inorganic anions (Figure 3d). Only a slight decay was observed in the presence of $H_2PO_4^{2-}$, possibly due to the quenching effect of the additive anions on $SO_4^{\bullet-}$ or $^{\bullet}OH$. More importantly, the high removal efficiency of CIP was achieved in various water systems (tap water and river water) (Figure S16a).

The PMS activation ability of Co–N_3O_1–1 was further evaluated by the degradation of multiple contaminants (e.g., sulfamethoxazole, tetracycline, and phenol) (Figure 3e). All contaminants were completely decomposed by Co–N_3O_1–1/PMS system in 20 min. Increasing the catalyst dosage or PMS concentration both improved the catalytic efficiency, indicating the high utilization efficiency of Co–N_3O_1–1/PMS system (Figure S16b,c). Based on the PMS decomposition experiments, the PMS decomposition efficiency reached 71.68 % and 89.71 % for Co–N_3O_1–1 and Co–N_3O_1–2, respectively (Figure S16d). All the above analyses suggested that Co–N_3O_1 was a promising PMS activator, in which the specific interaction between single Co atoms and oxygen-doped tubular C_3N_4 provided an accelerated activation pathway compared to Co^{2+} ions (homogeneous process) and Co–N_4 moiety (heterogeneous process).

Engineering the coordination environment of single atoms has been proved as an efficient strategy to selectively generate active radicals.[14b] To identify the dominated active species generated in these systems, radical quenching experiments were employed. ESR characterizations were employed as a direct monitor by using TEMP and DMPO as trapping agents. As shown in Figure 3g, the intensity of the triplet signals of TEMO-$^1O_2$ in Co–N_3O_1/PMS system was significantly enhanced compared to Co–N_4/PMS system. Furthermore, only DMPO-$^{\bullet}$OH and slight DMPO–$O_2^{\bullet-}$ were detectable in Co–N_4/PMS system, indicating that Co–N_3O_1/PMS system was highly selective to generate $^1O_2$, which was further proved by the radical quenching experiments. When TBA, methanol and BQ were added into the Co–N_3O_1 reaction process, only a negligible inhibition ratio of CIP decomposition could be observed (Figure 3f). Furthermore, L-histidine and NaN_3 significantly inhibited the CIP decomposition, and the higher concentrations of L-histidine and NaN_3 could cause a higher inhibition effect (Figure S17a). In the contrast, both TBA and methanol significantly inhibited the CIP degradation in the Co–N_4/PMS system, while L-histidine had a weak effect on the reaction process. With the structure change from Co–N_4 moiety to Co–N_3O_1 moiety, the inhibition of L-histidine increased from 35.28 % to 63.05 %, while the inhibition of TBA decreased from 78.71 % to 6.73 % (Figure 3e). Note that other factors such as the interaction between PMS and L-histidine,[33] PMS self-decomposition,[31] electron transfer[4,34] et al. could have an impact on the degradation process. Throughout a series of experiment under different conditions (Figure S17 and S18), we further identified that $^1O_2$ were dominant radicals and the origin relied on PMS activation by Co–N_3O_1. These findings confirmed that incorporation of oxygen atoms into Co–SACs local coordination environment favored selective generation of $^1O_2$.

The possible pathway towards selective $^1O_2$ production mechanism was further explored by the DFT computations. Based on the new insights into the activation of PMS towards $^1O_2$ production, we focused on two different reaction intermediates.[19b] The first pathway was the loss of the H atom to generate SO_5* and then the SO_5* rapidly self-reaction to produce $^1O_2$, SO_4^{2-} and $S_2O_8^{2-}$. In another pathway, the PMS was divided into SO_4* and OH* moieties.

The free energy profiles demonstrated that PMS→PMS*→ SO_4* and OH* were more thermodynamically favorable (Figure 4a). Bader charge change of divided SO_4* and OH*(1.41 e^-) was much more than that of divided SO_5* and H*(1.06 e^-), confirming the second pathway allowed donating more electrons to adsorbed PMS (Figure 4b, Table S7), which was also proved by LSV analyses (Figure S19). The results of the decreased current indicated that electrons transferred from a single Co atom to PMS. Compared to the Co–N_4 moiety, the changed current density of Co–N_3O_1–1 was much higher, suggesting that Co–N_3O_1–1 manifested a better conductivity for electron migration and possessed a faster reaction rate.[6] Furthermore, the charge state of the cobalt atom in Co–SO_4* (active sites) became more positive by 0.05 e^- in comparison with Co–SO_5*, hinting that SO_4* and OH* could slightly increase the charge state of the cobalt atom.[14b]

To distinguish the different selectivity towards reactive species generation between Co–N_3O_1 and Co–N_4, optimized potential free energy diagrams for the $^1O_2$ generation were then shown in Figure 4c,d, namely, PMS→PMS*→SO_4*+OH*→OH*+H_2SO_4→2OH*→O*→2O*→$^1O_2$. For this

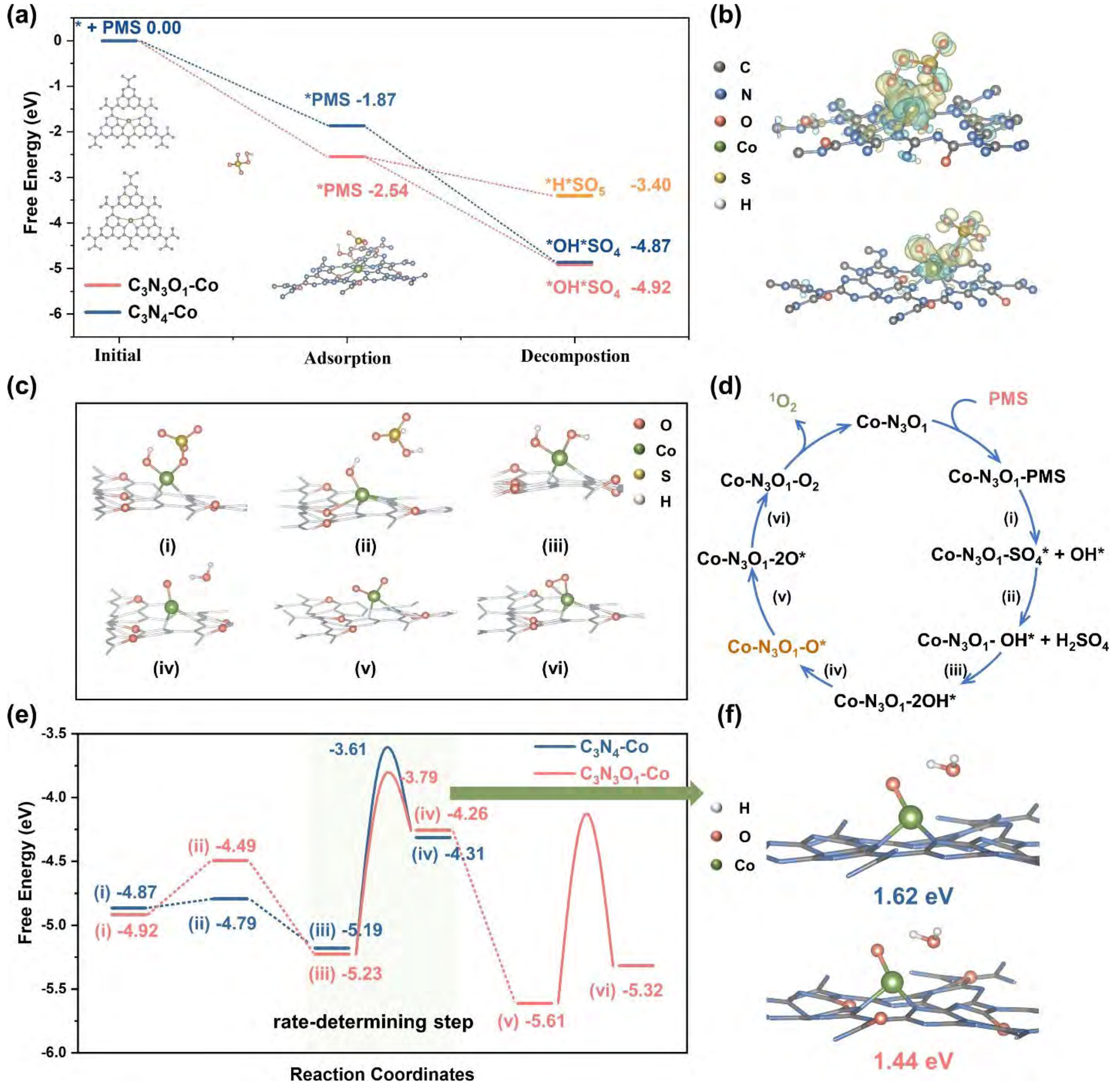

Figure 4. Proposed mechanism of $^1O_2$ generation over Co–N_3O_1 via PMS activation by DFT methods. a) Calculated potential energy diagrams for PMS decomposition to two key reaction intermediates and Gibbs free energy comparison of Co–N_3O_1 and Co–N_4 towards PMS adsorption. b) Bader charge analysis of two key reaction intermediates on Co–N_3O_1. c) The corresponding structures of reaction intermediates for proposed reaction process. d) Proposed reaction process for SO_4* and OH* moieties oxidation to $^1O_2$ on Co–N_3O_1 catalysts. e) The calculated potential energy diagrams for the rate-determining step and transition state based on SO_4* and OH* moieties oxidation to $^1O_2$ on Co–N_3O_1 and Co–N_4 catalysts. f) The kinetic barriers for 2*OH to *O on Co–N_3O_1 and Co–N_4 catalysts.

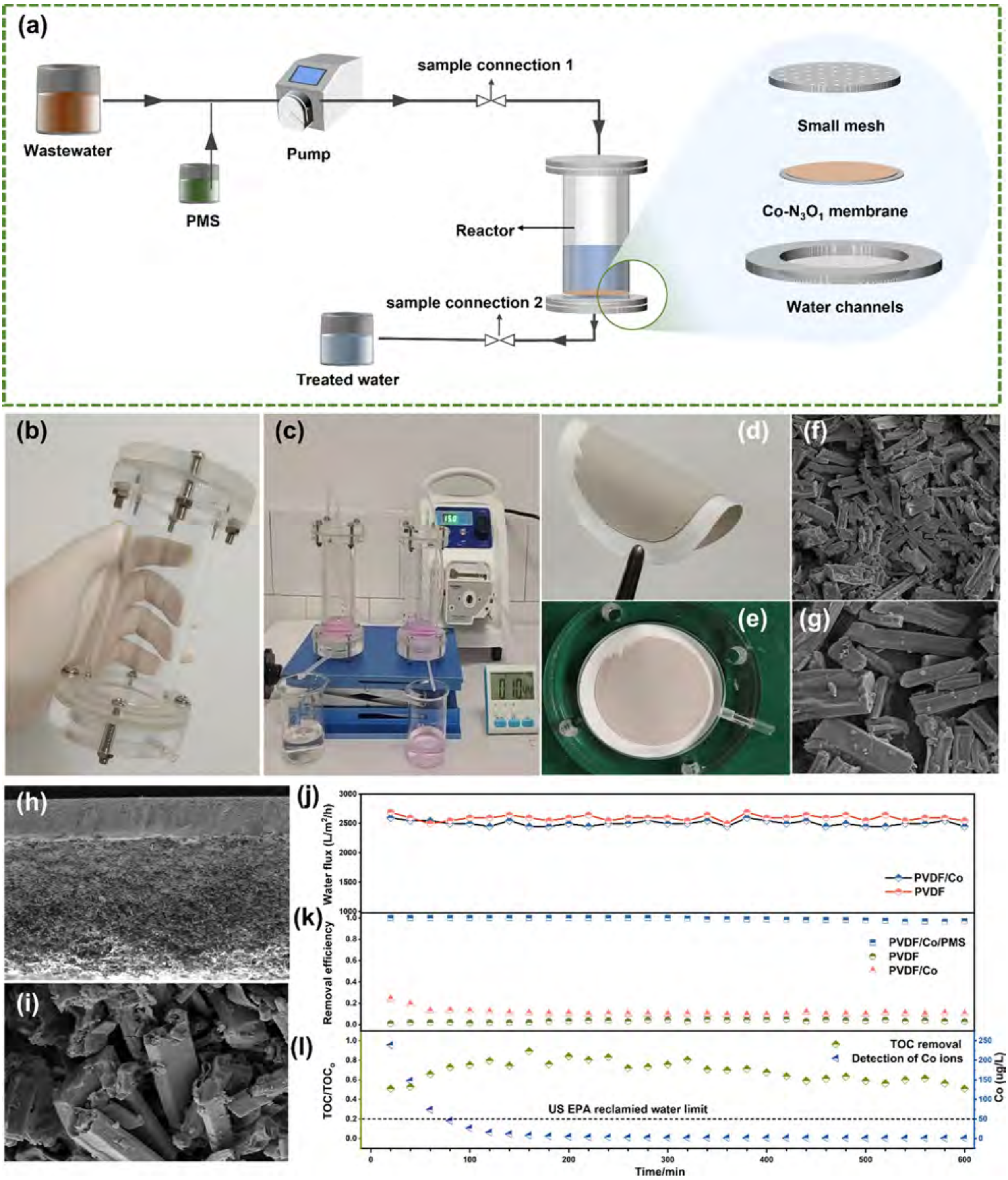

Figure 5. Preparation of Co–N$_3$O$_1$ membranes and application in water treatment via a continuous flow system. a) Schematic illustration of wastewater treatment process. b), c) Photograph of experiment device. To act as a proof-of-concept, the CIP was replaced as RhB for better observation. d), e) Photograph of the prepared Co–N$_3$O$_1$ membranes with an area of 12.56 cm^2 and the membrane exhibited high flexibility. f), g) SEM images of membrane surfaces. h), i) Cross-sectional scanning electron micrographs of membrane. j) The water performance of Co–N$_3$O$_1$ membranes and pristine membranes. k) CIP removal efficiency using Co–N$_3$O$_1$ membranes and pristine membranes. l) TOC removal and Co concentration in effluent as functions of filtration time.

typical pathway, the OH* was adsorbed on the single Co atoms site while SO_4* was employed to form H_2SO_4 via an exothermic reaction. In this step, Co–N$_4$ moiety presented reaction energy of −4.79 eV compared to that for Co–N$_3$O$_1$

of −4.49 eV, demonstrating that $SO_4^{\bullet -}$ may play more important roles under the effects of O atoms (Figure 4e). Furthermore, both the free energy diagram of Co–N_3O_1 and Co–N_4 moiety showed the largest energy barrier for the *O intermediate formation during the multistep $^1O_2$ generation process, indicating the formation of *O intermediate was a rate-determining step. After oxygen incorporation, the energy barrier regarding *O intermediate formation of *O intermediate was reduced from 1.62 eV to 1.44 eV, accounting for the promoted $^1O_2$ generation energetics (Figure 4f). The above theoretical results revealed that incorporation of oxygen atoms into the coordination environment of single Co atoms would alter the electronic structure of Co centers, thus contributing to promoting adsorption of PMS molecules and thermodynamically generating *O intermediate toward fast and selective $^1O_2$ generation.

Given the excellent catalytic performance of Co–N_3O_1/PMS system, it was further used in a practical application (Figure 5a–c). Membrane technology has created a bright future for supplying clean water resources due to its sustainability and convenience compared to dispersed catalyst suspensions.[35] The Co–N_3O_1 membranes were fabricated by vacuum-assisted filtering Co–N_3O_1 suspensions via PVDF substrate, namely PVDF/Co (Figure 5d, e). As shown in Figure 5f, g, the PVDF/Co was flexible and elastic. SEM images displayed that the random stacking of Co–N_3O_1 without obvious cracks and the cross-sectional SEM images indicated the PVDF/Co membranes had a thickness of about 217 μm with accessible 2D pinholes (Figure 5h, i). These abundant self-tubular structures with nanoholes can be employed as efficient water transfer channels, supplying full active catalytic sites for rapid permeation and purification of polluted water.

We firstly investigated CIP effluents permeances of PVDF and PVDF/Co to evaluate the transfer mass feature and rejection efficiency of target pollutant. The long-term performance was conducted by 30 cyclic tests over 10 h. The pristine membrane showed a water performance of 2594.29 $L m^{-2} h^{-1}$ accompanied by nearly 3.41 % (average) rejection over 10 h. Comparatively, PVDF/Co gave similar water permeance of 2502.85 $L m^{-2} h^{-1}$ accompanied by nearly 11.30 % (average) rejection, respectively (Figure 5j). These indicated that Co–N_3O_1 were efficient building blocks for water transportation and pollutants separation. After the addition of PMS, the removal of CIP in PVDF/Co system maintained 97.5 % over 10 h (Figure 5k), and the retention time of effluents in the PVDF/Co was only 312 ms (Figure S20), suggesting the high activity of PVDF/Co towards PMS activation.

Another advantage of PVDF/Co–based reactors lied in their leaching resistance and mineralization ability. As shown in Figure 5l, the detected Co concentration in the PVDF/Co/PMS system was at a state of 46.096 $\mu g L^{-1}$ after the fourth cycle, which was lower than the limitation of reclaimed water set by the US Environmental Protection Agency (50 $\mu g L^{-1}$). In the last few cycles, the detection leaching was below the 1 $\mu g L^{-1}$, suggesting the strong coordination between single Co atoms and C_3N_4. The TOC removal efficiency in the effluent was more than 51.10 % throughout the process of PVDF/Co/PMS experiment, indicating the excellent oxidation of the CIP molecules.

Conclusion

The modulation of coordination environment and design of support architectures can be adopted as new design principles for SACs toward PMS activation. In this study, the Co–N_3O_1 moiety anchored on TCN combined the advantages of PMS activation and selective $^1O_2$ generation process with robust stability. The single-atom catalyst achieved a high k value of 7.61×10^5 $min^{-1} mol^{-1}$ and TOF of 0.014 s^{-1}. Further integration of Co–N_3O_1 into membrane separation technology achieved high rejections (>97 %) toward pollutants with water permeances of 2502.85 $L m^{-2} h^{-1}$ above. Experiment and theoretical calculations revealed that the high PMS activation and selectivity for $^1O_2$ generation correlated with the incorporation of oxygen atoms into Co–SACs sites and morphology modulation, which resulted in the enhanced adsorption energy of PMS, enlarged contact surface area, and reduced activation barriers for $^1O_2$ generation. These findings provide a novel design principle for single-atom-based nanomaterials and highlight the reaction mechanism of PMS activation at the molecular level.

Acknowledgements

This work was supported by the National Natural Science Foundation of China (82003363, 82073449, U20A20323, 51521006, 52070077), the National Program for Support of Top-Notch Young Professionals of China (2014), the Program for Changjiang Scholars and Innovative Research Team in University (IRT-13R17), the Three Gorges Follow-up Research Project (2017HXXY-05), the National Natural Science Foundation of Changsha (kq2007059) and Hunan Graduate Innovation Project (QL20210097).

Conflict of Interest

The authors declare no conflict of interest.

Data Availability Statement

The data that support the findings of this study are available from the corresponding author upon reasonable request.

Keywords: Carbon Nitride · Coordination Environment · Peroxymonosulfate Activation · Single-Atom Catalysts · Wastewater Treatment

---

[1] a) Q. Q. Zhang, G. G. Ying, C. G. Pan, Y. S. Liu, J. L. Zhao, *Environ. Sci. Technol.* **2015**, *49*, 6772–6782; b) T. U. Berendonk, C. M. Manaia, C. Merlin, D. Fatta-Kassinos, E. Cytryn,

F. Walsh, H. Bürgmann, H. Sørum, M. Norström, M.-N. Pons, N. Kreuzinger, P. Huovinen, S. Stefani, T. Schwartz, V. Kisand, F. Baquero, J. L. Martinez, *Nat. Rev. Microbiol.* **2015**, *13*, 310–317.

[2] J. Lee, U. von Gunten, J. H. Kim, *Environ. Sci. Technol.* **2020**, *54*, 3064–3081.

[3] B. C. Hodges, E. L. Cates, J. H. Kim, *Nat. Nanotechnol.* **2018**, *13*, 642–650.

[4] W. Ren, C. Cheng, P. Shao, X. Luo, H. Zhang, S. Wang, X. Duan, *Environ. Sci. Technol.* **2022**, *56*, 78–97.

[5] a) X. Cheng, H. Guo, Y. Zhang, G. V. Korshin, B. Yang, *Water Res.* **2019**, *157*, 406–414; b) E. T. Yun, J. H. Lee, J. Kim, H. D. Park, J. Lee, *Environ. Sci. Technol.* **2018**, *52*, 7032–7042.

[6] W. Ren, G. Nie, P. Zhou, H. Zhang, X. Duan, S. Wang, *Environ. Sci. Technol.* **2020**, *54*, 6438–6447.

[7] L. Du, W. Xu, S. Liu, X. Li, D. Huang, X. Tan, Y. Liu, *J. Colloid Interface Sci.* **2020**, *577*, 419–430.

[8] Y. Gao, C. Yang, M. Zhou, C. He, S. Cao, Y. Long, S. Li, Y. Lin, P. Zhu, C. Cheng, *Small* **2020**, *16*, 2005060.

[9] a) Y. Shang, X. Xu, B. Gao, S. Wang, X. Duan, *Chem. Soc. Rev.* **2021**, *50*, 5281–5322; b) N. Zhang, C. Ye, H. Yan, L. Li, H. He, D. Wang, Y. Li, *Nano Res.* **2020**, *13*, 3165–3182.

[10] a) Z. Huang, Y. Yao, J. Lu, C. Chen, W. Lu, S. Huang, W. Chen, *J. Hazard. Mater.* **2016**, *301*, 214–221; b) P. Huang, J. Huang, S. A. Pantovich, A. D. Carl, T. G. Fenton, C. A. Caputo, R. L. Grimm, A. I. Frenkel, G. Li, *J. Am. Chem. Soc.* **2018**, *140*, 16042–16047; c) X. Li, X. Huang, S. Xi, S. Miao, J. Ding, W. Cai, S. Liu, X. Yang, H. Yang, J. Gao, J. Wang, Y. Huang, T. Zhang, B. Liu, *J. Am. Chem. Soc.* **2018**, *140*, 12469–12475; d) H. Xu, N. Jiang, D. Wang, L. Wang, Y. Song, Z. Chen, J. Ma, T. Zhang, *Appl. Catal. B* **2020**, *263*, 118350; e) Y. Yang, G. Zeng, D. Huang, C. Zhang, D. He, C. Zhou, W. Wang, W. Xiong, B. Song, H. Yi, S. Ye, X. Ren, *Small* **2020**, *16*, 2001634.

[11] C. Chu, J. Yang, X. Zhou, D. Huang, H. Qi, S. Weon, J. Li, M. Elimelech, A. Wang, J. H. Kim, *Environ. Sci. Technol.* **2021**, *55*, 1242–1250.

[12] X. Mi, P. Wang, S. Xu, L. Su, H. Zhong, H. Wang, Y. Li, S. Zhan, *Angew. Chem. Int. Ed.* **2021**, *60*, 4588–4593; *Angew. Chem.* **2021**, *133*, 4638–4643.

[13] a) X. Wu, H. B. Zhang, S. W. Zuo, J. C. Dong, Y. Li, J. Zhang, Y. Han, *Nano-Micro Lett.* **2021**, *13*, 136; b) L. Liu, A. Corma, *Chem. Rev.* **2018**, *118*, 4981–5079.

[14] a) X. Dong, Z. Chen, A. Tang, D. D. Dionysiou, H. Yang, *Adv. Funct. Mater.* **2022**, *32*, 2111565; b) H. Jin, P. Li, P. Cui, J. Shi, W. Zhou, X. Yu, W. Song, C. Cao, *Nat. Commun.* **2022**, *13*, 723.

[15] a) Y. Wu, C. Chen, X. Yan, X. Sun, Q. Zhu, P. Li, Y. Li, S. Liu, J. Ma, Y. Huang, B. Han, *Angew. Chem. Int. Ed.* **2021**, *60*, 20803–20810; *Angew. Chem.* **2021**, *133*, 20971–20978; b) C. Tang, Y. Jiao, B. Shi, J. N. Liu, Z. Xie, X. Chen, Q. Zhang, S. Z. Qiao, *Angew. Chem. Int. Ed.* **2020**, *59*, 9171–9176; *Angew. Chem.* **2020**, *132*, 9256–9261; c) J. Zhang, Y. Zhao, C. Chen, Y. C. Huang, C. L. Dong, C. J. Chen, R. S. Liu, C. Wang, K. Yan, Y. Li, G. Wang, *J. Am. Chem. Soc.* **2019**, *141*, 20118–20126.

[16] E. Jung, H. Shin, B. H. Lee, V. Efremov, S. Lee, H. S. Lee, J. Kim, W. Hooch Antink, S. Park, K. S. Lee, S. P. Cho, J. S. Yoo, Y. E. Sung, T. Hyeon, *Nat. Mater.* **2020**, *19*, 436–442.

[17] C. Tang, L. Chen, H. Li, L. Li, Y. Jiao, Y. Zheng, H. Xu, K. Davey, S. Z. Qiao, *J. Am. Chem. Soc.* **2021**, *143*, 7819–7827.

[18] L. Deng, L. Qiu, R. Hu, L. Yao, Z. Zheng, X. Ren, Y. Li, C. He, *Appl. Catal. B* **2022**, *305*, 121058.

[19] a) Y. Gao, Y. Zhu, L. Lyu, Q. Zeng, X. Xing, C. Hu, *Environ. Sci. Technol.* **2018**, *52*, 14371–14380; b) Y. Gao, T. Wu, C. Yang, C. Ma, Z. Zhao, Z. Wu, S. Cao, W. Geng, Y. Wang, Y. Yao, Y. Zhang, C. Cheng, *Angew. Chem. Int. Ed.* **2021**, *60*, 22513–22521; *Angew. Chem.* **2021**, *133*, 22687–22695.

[20] J. Wang, B. Li, Y. Li, X. Fan, F. Zhang, G. Zhang, W. Peng, *Adv. Sci.* **2021**, *8*, 2101824.

[21] P. Zhang, Y. Yang, X. Duan, Y. Liu, S. Wang, *ACS Catal.* **2021**, *11*, 11129–11159.

[22] B. Wu, L. Zhang, B. Jiang, Q. Li, C. Tian, Y. Xie, W. Li, H. Fu, *Angew. Chem. Int. Ed.* **2021**, *60*, 4815–4822; *Angew. Chem.* **2021**, *133*, 4865–4872.

[23] a) Y. S. Jun, J. Park, S. U. Lee, A. Thomas, W. H. Hong, G. D. Stucky, *Angew. Chem. Int. Ed.* **2013**, *52*, 11083–11087; *Angew. Chem.* **2013**, *125*, 11289–11293; b) J.-W. Zhang, S. Gong, N. Mahmood, L. Pan, X. Zhang, J.-J. Zou, *Appl. Catal. B* **2018**, *221*, 9–16.

[24] S. An, G. Zhang, T. Wang, W. Zhang, K. Li, C. Song, J. T. Miller, S. Miao, J. Wang, X. Guo, *ACS Nano* **2018**, *12*, 9441–9450.

[25] X. Hai, S. Xi, S. Mitchell, K. Harrath, H. Xu, D. F. Akl, D. Kong, J. Li, Z. Li, T. Sun, H. Yang, Y. Cui, C. Su, X. Zhao, J. Li, J. Perez-Ramirez, J. Lu, *Nat. Nanotechnol.* **2022**, *17*, 174–181.

[26] X. Xiao, Y. Gao, L. Zhang, J. Zhang, Q. Zhang, Q. Li, H. Bao, J. Zhou, S. Miao, N. Chen, J. Wang, B. Jiang, C. Tian, H. Fu, *Adv. Mater.* **2020**, *32*, 2003082.

[27] J. Li, B. Shen, Z. Hong, B. Lin, B. Gao, Y. Chen, *Chem. Commun.* **2012**, *48*, 12017–12019.

[28] Y. Zeng, X. Liu, C. Liu, L. Wang, Y. Xia, S. Zhang, S. Luo, Y. Pei, *Appl. Catal. B* **2018**, *224*, 1–9.

[29] C. Chu, Q. Zhu, Z. Pan, S. Gupta, D. Huang, Y. Du, S. Weon, Y. Wu, C. Muhich, E. Stavitski, K. Domen, J. H. Kim, *Proc. Natl. Acad. Sci. USA* **2020**, *117*, 6376–6382.

[30] a) C. Wang, S. Mao, Z. Wang, Y. Chen, W. Yuan, Y. Ou, H. Zhang, Y. Gong, Y. Wang, B. Mei, Z. Jiang, Y. Wang, *Chem* **2020**, *6*, 752–765; b) Y. Yin, L. Shi, W. Li, X. Li, H. Wu, Z. Ao, W. Tian, S. Liu, S. Wang, H. Sun, *Environ. Sci. Technol.* **2019**, *53*, 11391–11400.

[31] N. Li, R. Li, X. Duan, B. Yan, W. Liu, Z. Cheng, G. Chen, L. a Hou, S. Wang, *Environ. Sci. Technol.* **2021**, *55*, 16163–16174.

[32] Z. Wang, H. Wang, Z. Zeng, G. Zeng, P. Xu, R. Xiao, D. Huang, X. Chen, L. He, C. Zhou, Y. Yang, Z. Wang, W. Wang, W. Xiong, *Appl. Catal. B* **2020**, *267*, 118700.

[33] Y. Gao, Z. Chen, Y. Zhu, T. Li, C. Hu, *Environ. Sci. Technol.* **2020**, *54*, 1232–1241.

[34] a) F. Chen, L. L. Liu, J. J. Chen, W. W. Li, Y. P. Chen, Y. J. Zhang, J. H. Wu, S. C. Mei, Q. Yang, H. Q. Yu, *Water Res.* **2021**, *191*, 116799; b) J. Wang, J. Yu, Q. Fu, H. Yang, Q. Tong, Z. Hao, G. Ouyang, *ACS Cent. Sci.* **2021**, *7*, 355–364.

[35] a) Y. Wu, C. F. Fu, Q. Huang, P. Zhang, P. Cui, J. Ran, J. Yang, T. Xu, *ACS Nano* **2021**, *15*, 7586–7595; b) J. Xu, X. Zheng, Z. Feng, Z. Lu, Z. Zhang, W. Huang, Y. Li, D. Vuckovic, Y. Li, S. Dai, G. Chen, K. Wang, H. Wang, J. K. Chen, W. Mitch, Y. Cui, *Nat. Sustainability* **2021**, *4*, 233–241; c) Y. Zou, K. Xiao, Q. Qin, J. W. Shi, T. Heil, Y. Markushyna, L. Jiang, M. Antonietti, A. Savateev, *ACS Nano* **2021**, *15*, 6551–6561.

Manuscript received: February 12, 2022
Accepted manuscript online: May 5, 2022
Version of record online: ■■, ■■

Research Articles

Advanced Oxidation Processes

Z. Wang, E. Almatrafi, H. Wang, H. Qin, W. Wang, L. Du, S. Chen, G. Zeng,* P. Xu* ______________ **e202202338**

Cobalt Single Atoms Anchored on Oxygen-Doped Tubular Carbon Nitride for Efficient Peroxymonosulfate Activation: Simultaneous Coordination Structure and Morphology Modulation

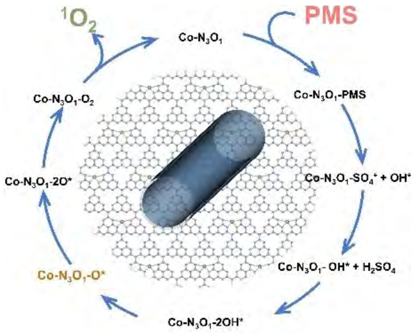

A synthetic method was developed to modulate the coordination environment and regulate support architecture, thus incorporating oxygen atoms into the first shell of Co single-atom catalysts (SACs). The high activity and $^1O_2$ selectivity of Co–N_3O_1 correlated with an enhanced adsorption energy of peroxymonosulfate (PMS) and reduced activation barriers. As a result, the catalysts were attached to a membrane to deliver a catalytic filter with 97.5 % ciprofloxacin rejection over 10 hours.